FULL PAPER

Three-Dimensional Inkjet-Printed Interconnects using Functional Metallic Nanoparticle Inks

*Jacob A. Sadie and Vivek Subramanian**

Inkjet-printed gold nanoparticle pillars are investigated as a high-performance alternative to conventional flip-chip interconnects for electronic packages, with significant advantages in terms of mechanical/chemical robustness and conductivity. The process parameters critical to pillar fabrication are described and highly uniform pillar arrays are demonstrated. More generally, this work underscores the impact of sintering on the electrical, mechanical, structural, and compositional properties of three-dimensional nanoparticle-based structures. Using heat treatments as low as 200 °C, electrical and mechanical performance that outcompetes conventional lead-tin eutectic solder materials is achieved. With sintering conditions reaching 300 °C it is possible to achieve pillars with properties comparable to bulk gold. This work demonstrates the immense potential for both inkjet printing and metal nanoparticles to become a viable and cost-saving alternative to both conventional electronic packaging processes and application-specific integration schemes.

1. Introduction

Inkjet printing functional electronic inks has proven to be a powerful alternative to conventional fabrication techniques for various applications.[1–6] Not only does droplet-on-demand inkjet printing offer characteristics ideal for manufacturability—it is non-contact, additive, adaptive-on-the-fly, and has the potential for high-throughput processing via the coordination of massively parallel arrays of inkjet nozzles—but it also enables the fabrication of structures on non-traditional electronic substrates and facilitates the use of nanostructured materials as a means of reducing critical process temperatures while still achieving high-performance features. However, the printing of functional inks has generally been confined to the two-dimensional world of thin-film devices; much effort has been focused on the fabrication of passive components,[1,2] thin-film transistors,[3] sensors,[4,5] solar cells,[6] and so forth, while little progress has been made in exploring the third dimension with these promising materials. Given the recent surge in three-dimensional printing processes, the time is ripe for identifying the applications, developing the processes, and understanding the mechanisms that dictate performance of electronically functional three-dimensional inkjet-printed structures.

The primary limitation of the application space will be the critical dimension of inkjet printing technology—which is on the order of ten microns. While this dimension seems large when compared to the nanoscale limits of conventional lithography, it is an ideal fit for MEMS, sensor, and integrated circuit package interconnects. Further, this application space will continue to bloom as demand continues for flexible, thin, mobile, wearable, and ubiquitous electronics; this is evidenced, for example, by the proliferation in chip stacked packages in mobile phones.[7] The primary challenge is the exploration of functional inks (i.e. metallic, semiconducting, and dielectric inks) with the specific goal of fulfilling the growing demand for the various aforementioned arenas. For example, metallic nanoparticle inks have already demonstrated the potential for achieving high conductivity interconnects at processing temperatures as low at 150 °C.[8] However, these properties are achieved with films less than 1 μm thick. Understanding the implications of fabricating features tens of microns tall yet still comprised of these nanoscale structures will be critical to determining the utility of such novel materials in 3D applications.

With specific regard to package interconnects, the main driver is the unrelenting demand of CMOS scaling (see **Figure 1**), which is demanding smaller, more closely-spaced, and more total interconnects per package. Furthermore, growing health concerns as well as performance/reliability issues related to thermal conductivity, electric conductivity, and electromigration failure of conventional lead-tin eutectic interconnect materials have led to a search for replacements. To date, only gold stud bumps and solder-capped copper posts have gained significant traction.[9–13] While the conductivity of these interconnects will unquestionably outperform eutectics, there are a number of drawbacks associated with the required fabrication process steps. First, gold bumping is a relatively low-throughout processes requiring thermosonic bonding, which is very sensitive to process parameters and often leads to bump deformation/poor bond strength.[14] Second, the copper processes (and some gold processes) rely on electroplating, which both introduces multiple processing steps and results in large volumes of wasted material. Due to these tradeoffs between material properties and fabrication costs, it is vital that new fabrication techniques and new functional materials be explored

J. A. Sadie, V. Subramanian
Department of Electrical Engineering and Computer Sciences
University of California, Berkeley,
Berkeley, CA 94720–1770, USA
E-mail: viveks@eecs.berkeley.edu

DOI: 10.1002/adfm.201401312

© 2014 WILEY-VCH Verlag GmbH & Co. KGaA, Weinheim

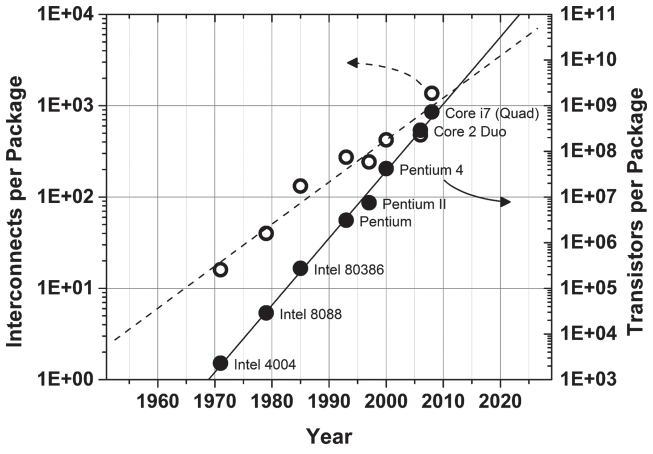

Figure 1. Exponential growth of transistors and interconnects per package for select Intel processors since 1970.

in an effort to minimize cost and maximize performance. To that end, this work explores the viability of three-dimensional droplet-on-demand inkjet printing of metal nanoparticle inks for the fabrication of packaging vertical interconnects.

Metal nanoparticle inks, typically comprised of organic-encapsulated nanoparticles suspended in solution,[8,15–17] are an ideal choice for package interconnects as well as general three-dimensional conductive structures. First, because the melting point of the nanoscale materials is dramatically reduced due to the increased surface area-to-volume ratio as compared to bulk,[18] the sintering temperatures of materials is often below the thermal budgets of standard processes and below the glass transition temperature of several attractive polymer substrates. In addition, many existing sintering techniques such as intense pulsed light,[19] microwave,[20] electrical,[21] and so on, may offer even further improvements to thermal constraints. Finally, a specific concern in package interconnects is electromigration; however these materials have also demonstrated superior electromigration performance.[22]

While many solution-based deposition techniques exist, inkjet printing is a particularly attractive three-dimensional deposition technique for these specific interconnect structures. First, the ten micron critical dimension of inkjet printing matches well with the current and future technology node requirements for package interconnects.[23] In addition, the application of metal nanoparticle inks offers the opportunity to fabricate structures that readily compete with conventional materials with regard to their performance metrics. While we have recently reported on the inkjet fabrication of such features,[24] much of the work toward printed, conductive, three-dimensional interconnects that does exist emphasizes demonstrations of electrohydrodynamic printing,[25] extrusion printing,[26] and molten solder droplet printing.[27] While these techniques have their own advantages and drawbacks, none offer the scalability, throughput, and performance of inkjet-printed nanoparticles. To our knowledge, this work is the first complete study of the electrical and mechanical properties critical to high performance of such large nanoparticle-based structures and the results discussed herein will serve to further motivate the research of materials, processes, and applications for functional three-dimensional structures.

2. Results and Discussion

2.1. Printing Process

For a single nozzle, the volumetric flow rate of material ejected (Q_{drop}) is dictated by the drop frequency (f_{drop}) and the volume of an ejected droplet (V_{drop}). It is important to note that 1) V_{drop} includes the solvent volume (V_{solv}) and nanoparticle volume (V_{NP}), and 2) generally V_{solv} is much greater than V_{NP} due to the need to maintain low ink viscosity. Consequently, assuming V_{drop} is constant over the course of printing, the main control over Q_{drop} becomes f_{drop}.

Because the primary constituent of the droplet is the solvent material, wetting/spreading of the ink on the substrate typically makes it difficult to print high aspect ratio features. To control this spreading, we print at elevated substrate temperature, causing the evaporation of the solvent prior to the next drop impinging on the surface. This evaporation rate (Q_{evap}) is dictated by the solvent material and the substrate temperature (T_{sub}). For a given ink system, the solvent is constant, making T_{sub} the primary control for Q_{evap}.

Figure 2 demonstrates the impact of each of these process parameters. All samples prepared in Figure 2a were fabricated with a total of 50 drops and images were taken before any sintering occurred. The volumetric flow rates for these pillars range from ≈20–60 pL/s as the applied drop frequency is adjusted from 0.16 Hz to 0.5 Hz. As f_{drop} increases and T_{sub} is held constant, it becomes increasingly difficult to build vertical features because Q_{evap} is much less than Q_{drop}. The result is a short and continuously expanding dome-shaped puddle on the substrate. However, increasing T_{sub} at a given f_{drop} results in increasing Q_{evap} such that tall, narrow pillars are able to form. Figure 2a demonstrates this shift in morphology and Figure 2b is an enhanced view of a pillar printed with 30 total drops.

Extracting the height and width measurements from these printed pillars, we can determine the aspect ratio of these pillars as a function of printing conditions (Figure 2c). For the high f_{drop}, low T_{sub} conditions it was not possible to measure an accurate height or width, so the aspect ratios of these samples are omitted from Figure 2c. As demonstrated, pillars with an aspect ratio of approximately 6:1 can be fabricated with as few as 50 droplets.

The formation of these pillars involves three distinct regimes, which we name wetting, tapering, and growth. In the wetting regime, the initial droplet wets the substrate and expands to essentially the same diameter regardless of print condition. A higher T_{sub} may eventually result in decreasing this initial spreading, though this was not observed in our experiments. During the tapering regime, as more droplets impinge upon the substrate they slowly begin to pin with a smaller diameter until a final, steady-state diameter is reached. Finally, throughout the growth regime, subsequent droplets contribute solely to increasing the height of the pillar. Assuming Q_{drop} and Q_{evap} remain constant, the height of the pillar should increase linearly and the width remain constant, allowing for very high aspect ratio features to be fabricated simply by adding to the total number of drops. This assumption may break down as pillars grow taller because the temperature at the top of the

© 2014 WILEY-VCH Verlag GmbH & Co. KGaA, Weinheim

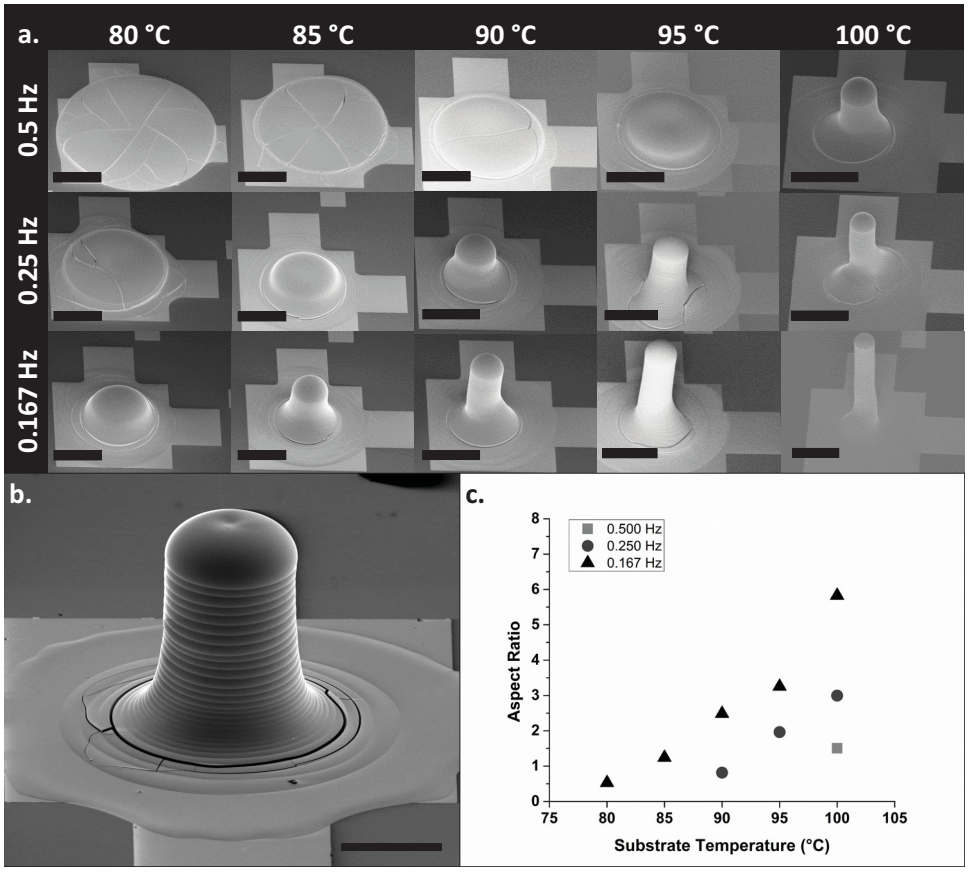

Figure 2. The impact of printing process parameters f_{drop} and T_{sub}. a) Higher T_{sub} and lower f_{drop} lead to higher aspect ratio pillars. b) Example of single printed pillar. c) Extracted aspect ratio from images in a). All printed pillars fabricated with a total of 50 drops. Scale bars in a) are 100 μm and in b) are 50 μm.

pillar may begin to decrease below T_{sub} if heat conduction from the bottom to the top of the pillar is too slow, however no issues became apparent during our fabrication process. Indeed, we have shown that incredible complex high-aspect ratio structures (see **Figure 3**a,b) such a vertical polygons and multi-branched "cacti" can be built using this approach; this attests to the promise of this technique for generalized 3D fabrication.

2.2. Coplanarity and Compaction

Conventional packaging interconnects depend on reflow bonding to compensate for package nonplanarity and die bow, that is, solder reflow allows for robust interconnection despite wide variation in gap height. Similarly, as-printed pillar coplanarity and post-sintering pillar compaction are important criteria for printed nanoparticle-based interconnects. Higher coplanarity results in minimized gap height variation prior to sintering and sintering-triggered pillar compaction will improve interconnection bonds similar to reflow processes with conventional materials. During thin film nanoparticle sintering, the encapsulant-metal bonds break, both the encapsulant material and the metal nanoparticles begin to diffuse, and nanoparticles eventually coalesce to form a continuous, compact, conductive, polycrystalline films.[2,16,17,19–21,28] Thus, we expect the pillars to compact upon sintering due to outdiffusion of the ligand, similar to the compaction observed in two-dimensional nanoparticle thin films.

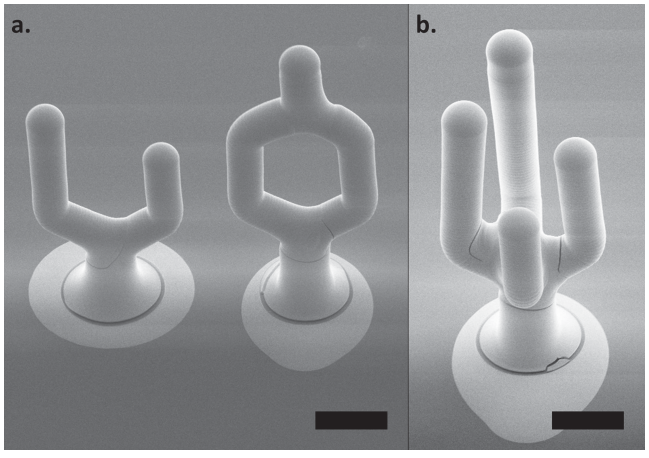

Figure 3. Demonstrations of generic high-aspect ratio structures fabricated with inkjet-printed gold nanoparticles. a) hexagonal structures and b) "cacti" with scale bars representing 100 μm in each micrograph.

© 2014 WILEY-VCH Verlag GmbH & Co. KGaA, Weinheim

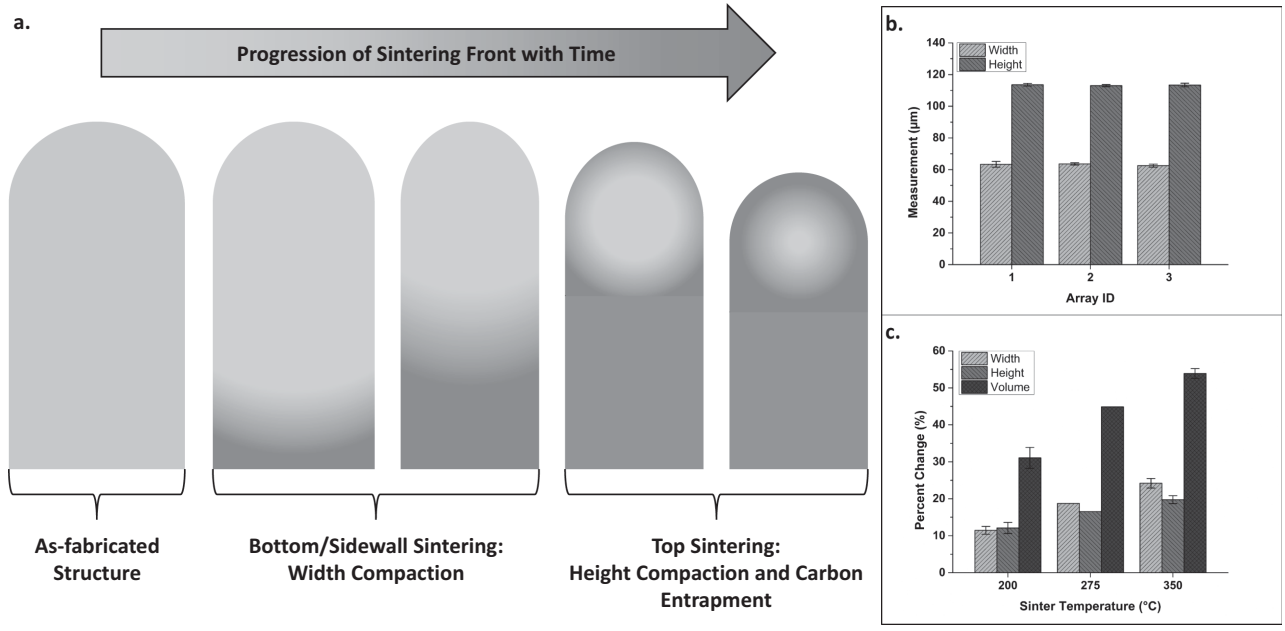

Figure 4. a) Schematic diagram depicting densification and compaction of nanoparticle-based pillars as a function of sintering time. The sintering front separates the dense, sintered (darker) material from the less dense, unsintered (lighter) material in the schematic. b) Pre-sintered height and width values for three arrays of printed pillars demonstrating highly coplanar structures. c) Height, width, and extracted volume compaction of pillars as a function of sinter temperature demonstrating pillar compaction during sintering. Error bars represent sample standard deviation. Coplanarity and compaction data extracted sintered pillars fabricated with a total of 30 drops each.

To measure this compaction we monitor the change in height and width as a function of sintering condition. Results are shown in **Figure 4**b,c.

We fabricated arrays of pillars with the following conditions: $f_{drop} = 0.125$ Hz, $T_{sub} = 110$ °C, and total drop count of 30 drops. The printed arrays were arranged in a rectangular grid with a large pitch of 650 μm, though it is worthwhile to note this pitch can be decreased to approximately 200 μm with relative ease, and, indeed, can be scaled further by reduction in jetted droplet size. The primary limit for minimizing the pitch of the printed arrays is the diameter of the first printed drop. Of the arrays printed, three separate arrays were measured to determine the height and width variation per array before sintering. The average across all samples was 113 μm tall and 63 μm in diameter, with a standard deviation of 0.90 μm and 1.21 μm, respectively. Thus, it is evident that the inkjet printing process is indeed highly reliable both within an individual printing process and across multiple processes.

In Figure 4c we present the effect of sintering temperature on extracted volume compaction of the pillars in our printed arrays. While sinter time and temperature will both play a role in determining the degree of pillar compaction, the effect of temperature is much stronger for the time and temperature ranges tested, thus only the effect of temperature is shown (see Supporting Information Table S1 for complete dataset). To determine the percent change in volume, we use the average value for the height and width of the pre-sintered pillars as an initial value and we model the shape of the pillar as a perfect cylinder. We see up to 53% volume reduction in pillars sintered at 350 °C (see Supporting Information Table S2 for complete dataset). The error bars representing standard deviation in Figure 4c appear to be large because various sintering times were included in determining the effect of temperature, however the average intra-array variation across all nine arrays was 1.27 μm and 0.95 μm for height and width, respectively. Therefore, both the pre- and post-sintering coplanarity values are highly uniform.

Figure 4a presents a schematic cross-section of pillars throughout the sintering process. Special attention should be paid to the location of the sintering front which represents a boundary between densely sintered nanoparticle material and the less dense regions that still contain large amounts of carbon. Because heat is applied at the base of the pillar during sintering, we expect sintering to initiate at the base of the pillar and extend upward through the pillar. In addition, we anticipate the thermal conductivity of sintered material to be higher than unsintered material due to the densification of the metal. This thermal conductivity increase will aid in accelerating sintering. Finally, we expect the center of the pillars to sinter the slowest due to the increased distance the free encapsulant must diffuse to escape the system and the potential for denser sintered material on the outside of the pillar to act as a barrier to diffusion. This implies both a vertical and lateral diffusion of material during the sintering process, which will strongly impact the electrical and mechanical properties of the sintered structures. We will experimentally verify this view of 3D sintering below.

2.3. Electrical, Elastic, and Shear Properties

In general, we expect more extreme sintering treatments to result in extracted material properties closer to bulk properties. For example, ideal electrical performance would be a resistivity equal to bulk gold: 2.44 μΩ cm. However, large volumes

© 2014 WILEY-VCH Verlag GmbH & Co. KGaA, Weinheim

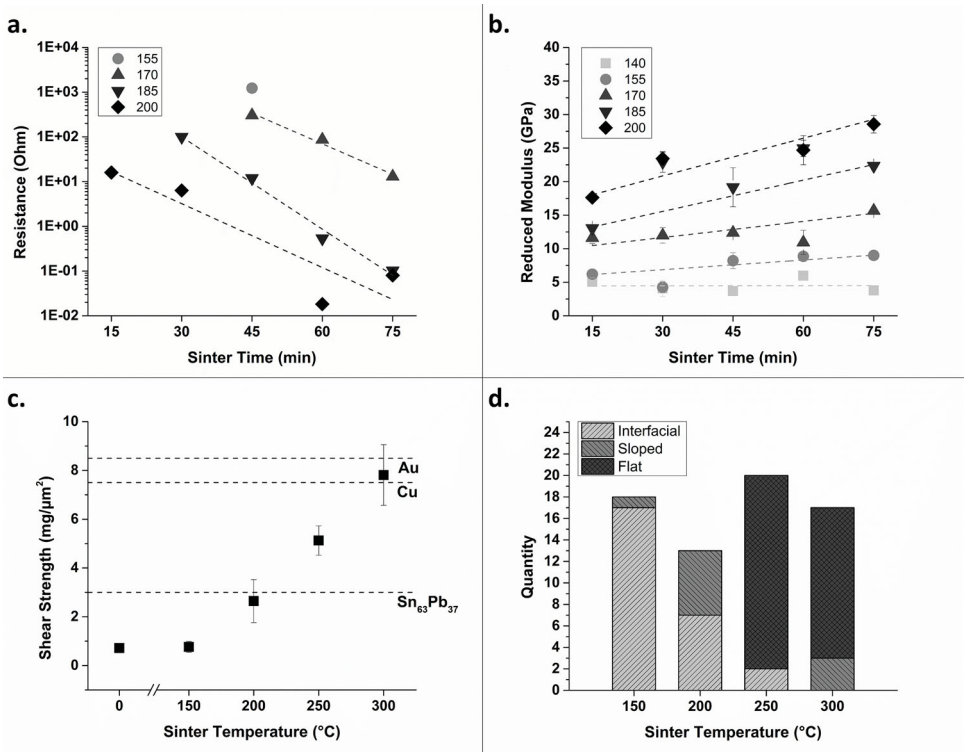

Figure 5. Pillar a) electrical and b) elastic property response as a function of sintering time and temperature. c) Shear strength and d) distribution of shear surface failure mechanisms as a function of sintering temperature for pillar arrays sintered for one hour. Horizontal bars in c) represent shear strengths guaranteed in industrial processes.

of residual encapsulant are detrimental to conductivity in two-dimensional nanoparticle films,[8,17] and the same response is expected for pillar structures. The electrical, mechanical, and shear response of these pillars as a function of sintering treatment is shown in **Figure 5**a–d.

First, Figure 5a presents the measured electrical performance of a set of pillars fabricated with 30 drops each and sintered between 140–200 °C for 15–75 min. Pillar resistance was extracted using the custom four-point probe technique described in the experimental section. As expected, an increase in sintering temperature as well as sintering time results in a decrease in measured resistance. It appears that the electrical response is exponentially dependent upon the sintering time, which we attribute to the diffusive nature of the free encapsulant material migrating within the system as the nanoparticles coalesce and the pillars compact. As the temperature increases, the diffusion rate is accelerated and the time to achieve high conductivity is decreased. The 140 °C and much of the 155 °C sintered samples do not appear on the plot because the resistance was beyond the measurable range. This indicates that at lower temperature and time conditions, the sintering and compaction of the nanoparticles has not yet created a conductive path from the base to the top of the pillar. Referring to the schematic drawn in Figure 4a, this would correspond to bottom and sidewall sintering but no sintering along the top of the pillar. The lowest resistivity measured in this experiment is 40.7 μΩ cm, but the lowest resistivity measured to date for pillars annealed at fully optimized conditions is 13.2 μΩ cm, or 16% of the conductivity of bulk gold and a higher conductivity than available from conventional eutectics.[29]

Using the same set of pillars, we performed nanoindentation tests to determine the elastic response of the pillars as a function of sintering conditions. The results are presented in Figure 5b. We first note that, unlike the electrical tests that resulted in nonconductive, that is, non-measurable, pillars for both the 140 °C and 155 °C conditions, we are able to measure all of the prepared pillars in this mechanical test. In fact, we observe little to no increase in elastic modulus for these minimally sintered pillars, which correlates well with the lack of a dense, sintered, conductive path reaching the top of the pillar. Similar to the electrical response, the elastic modulus increases as a function of time, which correlates with the compaction of the pillars and outdiffusion of encapsulant, and increasing the sinter temperature results in a shorter time to achieve high modulus. The peak elastic modulus measured is 28.6 GPa, which is 36% of the bulk gold modulus and comparable to conventional eutectics.

In addition to the electrical and elastic property extraction, a final shear test experiment was performed to determine the shear strength of sintered pillars; this is a particularly important test for semiconductor packaging applications, since shear strength is a standard specification requirement for semiconductor packages. New pillar arrays were fabricated and pillar compaction was recorded prior to shear testing to normalize shear strength to cross-sectional area. As shown in Figure 5c, when comparing the shear strength of unsintered pillars with pillars sintered at 150 °C, no clear effect is visible. However,

© 2014 WILEY-VCH Verlag GmbH & Co. KGaA, Weinheim

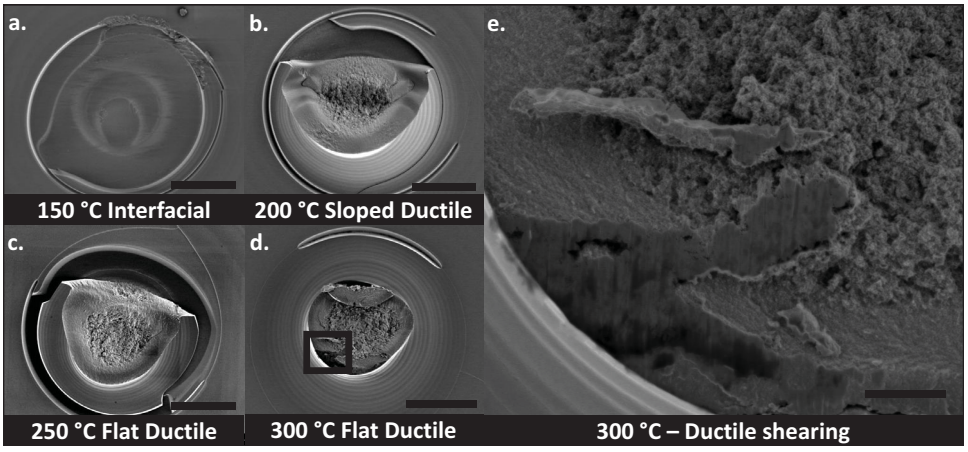

Figure 6. Shear failure interfaces. a–d) Shear surfaces for various sinter conditions. e) Enhanced view of sample d). Scale bars in (a–d) represent 40 μm and in (e) represent 5 μm.

increasing the temperature results in dramatically increasing shear strengths driven by the decrease in pillar diameter as well as improved strength of sintered gold. The shear failure mechanisms outlined in the JEDEC Solder Ball Shear standard are ductile, pad lift, ball lift, and interfacial break.[30] In our testing we primarily observe ductile and interfacial shearing. As a further level of distinction, we divide the ductile shearing into two categories: flat ductile and sloped ductile shearing. Figure 5d details the rate of shear failure mechanism as a function of sintering condition. The shear direction is bottom-up for all images. Interfacial shearing between the pillar and pad dominate low temperature sinter processes, indicating sintering has not successfully formed a solid bond across the pad. For the higher temperature conditions, flat ductile shear surfaces extend throughout the pillars. The intermediate sloped ductile failure mechanism primarily occurs in the 200 °C condition whereby pillar shear surfaces begin flat and suddenly slope downward once the center of the pillar is reached. Top-down SEM images are presented in **Figure 6**a–e depicting these failure mechanisms. At 300 °C we begin to see a shear response near the denser exterior of the pillar that resembles the ductile shear response of homogenous bulk materials (see Figure 6e). The average shear strength for the 300 °C sinter treatment is 7.81 mg μm^{-2}, which is 92% of the bulk gold shear strength guaranteed in industrial processes.[31] At 200 °C, the 2.64 mg μm^{-2} shear strength is comparable to conventional eutectic shear strength guaranteed in industrial processes.[30]

The time- and temperature-dependent nature of these pillar properties is a very important and promising outcome. First, with regard to absolute terms, the pillars fabricated and tested have achieved properties comparable to bulk materials at moderate heat treatments. This indicates the viability for such structures in applications where performance is paramount. Not only would the pillars presented in this work operate as electrical interconnects, but they would also outperform the conventional materials used for such an application. Second, and perhaps more importantly, the time- and temperature-dependent properties indicates these structures can be tuned to meet fairly precise design standards. Further, despite this work being focused strictly on metal nanoparticles, it is reasonable to expect other materials will exhibit similar tunability.

2.4. FIB and EDX

To validate the sintering model above, we perform structural and materials analysis as a function of sintering conditions. **Figure 7** shows cross-sections of three separate pillars sintered at varying time/temperature conditions and milled with FIB to elucidate the composition and structure of the features. There are stark qualitative differences between the gentle, moderate, and strong sintering conditions. First, the 150 °C and 175 °C pillars exhibit a typical "waterfall effect" which commonly occurs in composites with highly disparate atomic masses.[32] Because the main components of these pillars are carbon and gold, not only do the conditions needed for the observation of the waterfall effect apply but the severity of the waterfall effect may also be used as an indicator for residual carbon content. No waterfall effect is evident in the 200 °C sample, indicating a much smaller carbon content consistent with highly sintered samples. Additionally, as the sintering time and temperature increases, the large cracks within the structure disappear. This

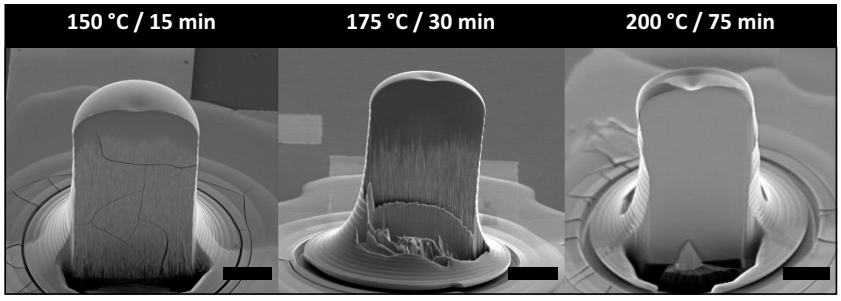

Figure 7. FIB milled pillars for various sinter time and temperature conditions. Waterfall effect and cracks diminish as sintering time and temperature increase. Scale bars represent 25 μm.

© 2014 WILEY-VCH Verlag GmbH & Co. KGaA, Weinheim

behavior is consistent with improved compaction as well as electrical and mechanical performance.

Because the 200 °C sintered pillar does not exhibit a strong waterfall effect, the surface was smooth enough to perform EDX scans. Prior to EDX, 10 pA polishing FIB scans were made to smooth the surface further. **Figure 8** shows the result of EDX scans throughout the pillar. At the base and center of the pillar the measured gold peak is about twice the intensity of the carbon peak, but the peaks are nearly equivalent at the top of the pillar, which indicates a higher carbon content at the top than the bottom. This is likely due to the pillar being primarily sintered from bottom to top as previously described. Furthermore, the field scans at the top of the pillar qualitatively indicate the carbon concentration is primarily located near the center of the pillar rather than the edge (see Figure S1, Supporting Information), consistent with the expectation that carbon in the center will take more time to diffuse out of the system due to the longer diffusion distances and the formation of a hard shell during the sintering process.

This structural and compositional characterization is the first direct investigation of sintering in such inherently large nanoparticle-based structures. The redistribution of carbon material within the pillar helps explain the electrical, elastic, and mechanical responses observed and helps to establish performance limitations for the given processing parameters. Namely, the entrapped carbon material within the final structure will contribute to a higher degree of elasticity as well as lower conductivity, and enhanced heat treatments will likely do little to permit the outdiffusion of the carbon through the dense shell-like structure. All of these results inform design decisions for optimized performance throughout the process: from encapsulant selection to printing parameters to sintering treatment.

3. Conclusion

We have demonstrated a well-controlled inkjet printing process for printing three-dimensional nanoparticle-based structures and we have explored the effects of sintering on critical structural properties. Both the printing process and sintering process result in well-controlled pillar arrays, suitable for use as vertical interconnects in semiconductor packaging applications. At process temperatures comparable to eutectic reflow temperatures, the pillars sinter and compact to achieve electrical and mechanical properties that outperform conventional eutectic

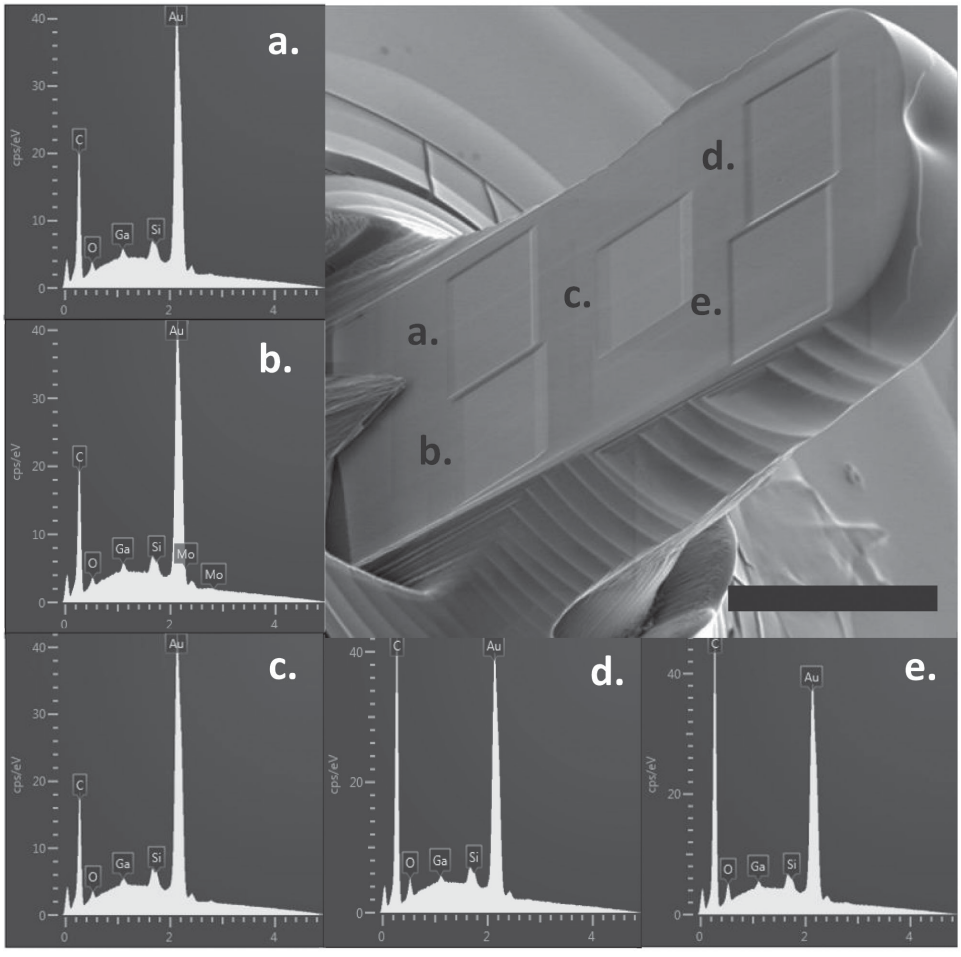

Figure 8. Polished sections of FIB milled pillar sintered at 200 °C for 75 min and corresponding EDX scans for each labeled area. EDX carbon-to-gold ratio increases moving upward throughout pillar indicated higher level of residual carbon content near top of pillar.

© 2014 WILEY-VCH Verlag GmbH & Co. KGaA, Weinheim

materials, indicating these features are clear competitors for eutectic solder replacement. Further, the general understanding of sintering and observation of encapsulant diffusion within these three-dimensional structures will provide invaluable insight for nanoparticle ink design to optimize performance at even lower temperatures and for new material systems. By demonstrating the success of metal nanoparticles, this work has made it quite clear that inkjet printing is a viable alternative to conventional, costly materials and processes for three-dimensional electronically functional structures.

4. Experimental Section

Inkjet Printing: All inkjet printing was performed on a custom-built droplet-on-demand inkjet printing system. The system is composed of *x*- and *y*-axis translational motors and a theta-axis controlled mounted stage. The stage has vacuum capability as well as heating/cooling control (up to 300 °C). Two cameras provide visual feedback of the printing process. MicroFab MJ-AT 60 μm orifice diameter nozzles are used for all printing experiments. A nitrogen-fed back pressure system with adjustable needle valves controls the meniscus of the fluid at the nozzle orifice above the stage. A personal computer controls all of these components and runs an original software suite to coordinate stage movements and drop ejections. The ink used in this work is a commercially available gold nanoparticle ink (Harima NPG-J) with typical viscosity ≈7 cP, density ≈1.8 g cm^{-3}, nanoparticle loading ≈55 wt%, and nanoparticle diameter ≈5 nm. Harima NPG-J has a primary nonaromatic solvent identified as "AF7" within the Materials Safety Data Sheet (MSDS) with a boiling point of ≈270 °C. Depending on the applied pulse waveform, the 60 μm nozzle produces drops with diameters that range between 55–65 μm and therefore produces drop volumes that range between 87–144 pL. A typical applied waveform is a standard bipolar pulse waveform with t_{dwell} = 20 μs, t_{echo} = 40 μs, V_0 = 0 V, V_+ = 19 V, V_- = –19 V, $t_{rise\text{-}1}$ = 3 μs, t_{fall} = 6 μs, and $t_{rise\text{-}2}$ = 3 μs to produce drops with calculated volumes of ≈100 pL. Any substrate temperature noted was allowed to settle before printing began to avoid temperature fluctuations during printing. Substrates used in all printing experiments are silicon test wafers with pre-patterned chrome/gold pads fabricated via standard photolithography, metal evaporation, and liftoff processes.

Sintering: All sintering experiments took place after the printed pillars were allowed to cool to room temperature after printing. Pillars were either sintered on the same heated stage as the one used for printing or in a one inch diameter tube furnace (which permits higher temperatures than the hotplate). The desired sintering temperature was allowed to reach its set point prior to placing the pillars on the stage or in the furnace. After the prescribed sintering time ended, samples were removed immediately and placed onto a cooling plate in order to quench the sintering process.

Electrical Characterization: Probing two pre-patterned extensions on the gold pad and carefully lowering another two probe tips onto the top of the pillar allows for a four-point probe measurement setup of the printed pillars. Multiple measurements were taken on each pillar, and the average extracted resistance was used to describe individual pillars. Error bars in relevant electrical characteristic plots indicate the standard deviation across multiple pillars printed and tested under the same conditions. To extract a material resistivity, we use a cylindrical approximation for the geometry of the pillars. An Agilent 4156B was used to record all measurements.

Mechanical Characterization: After printing and sintering were complete, nanoindentation tests performed at the top of the pillars were used to determine the reduced Young's modulus, E_r, of the pillars as a function of sintering condition. The load profile for each test includes a 1000 μN s^{-1} ramp to 5000 μN maximum force, a two second hold time, and a 1000 μN s^{-1} unloading segment. During unloading, force-displacement data is used to determine the reduced modulus of the sample. All tests were performed on a Hysitron TI 750 series TriboIndenter.

Shear Strength Characterization: Because most substrates used to print were very small (roughly 50 mm^2) compared to the bond tester stage, already-sintered substrates were affixed to glass microscope slides with a cyanoacrylate adhesive to prepare samples for bond testing. Samples rested overnight to fully harden before shear tests and care was taken to ensure the microscope slide did not slip during the test. Using a Nordson Dage 4000 bond tester, printed pillars were sheared at 100 μm s^{-1} at a height of 20–25 μm. Failure detection for tested pillars was set to a fallback of 30 percent, meaning a failure was recorded only if the measured force at any time dropped below 30 percent of the measured maximum force.

SEM, Optical, and EDX Characterization: Multiple instruments were used to image and characterize the morphology of printed pillars. Scanning electron microscope (SEM) images were obtained using both a Zeiss Leo SEM and FEI Quanta 3D FEG SEM. In addition, laser confocal microscopy with an Olympus LEXT OLS4000 was used to rapidly characterize the height and diameter of fabricated pillars. The brightness switching feature available on the confocal laser was necessary in order to successfully image the top surface of pillars. Finally, an FEI Quanta focused ion beam (FIB) and in situ energy-dispersive X-ray (EDX) spectroscopy tool were used to analyze the internal chemical composition of pillars as a function of sintering condition. A milling FIB current of 7 nA and a polishing FIB current of 10 pA were used to create surfaces for EDX scans.

Supporting Information

Supporting Information is available from the Wiley Online Library or from the author.

Acknowledgements

The authors would like to acknowledge Ultratech, Inc. for their financial support in funding this research effort. In addition, the authors acknowledge the Marvell Nanofabrication Laboratory and the Biomolecular Nanotechnology Center for access to their characterization resources and the Lawrence Berkeley National Laboratory for access to nanoindentation equipment. Finally, the authors would like to thank Steven Volkman for the many invaluable, thought-provoking discussions that influenced this work.

Received: April 23, 2014
Revised: June 7, 2014
Published online: September 11, 2014

[1] D. Redinger, S. Molesa, S. Yin, R. Farshi, V. Subramanian, *IEEE Tran. Electron Devices* **2004**, *51*, 1978.
[2] J. Perelaer, A. W. M. de Laat, C. E. Hendriks, U. S. Schubert, *J. Mater. Chem.* **2008**, *18*, 3209.
[3] V. Subramanian, T. Bakhishev, D. Redinger, S. K. Volkman, *J. Disp. Technol.* **2009**, *5*, 525.
[4] L. Jaggannathan, V. Subramanian, *Biosens. Bioelectron.* **2009**, *25*, 288.
[5] V. Correia, C. Caparros, C. Casella, L. Francesch, J. G. Rocha, S. Lanceros-Mendez, *Smart Mater. Struct.* **2013**, *22*, 105028.
[6] Y. Galagan, B. Zimmermann, E. W. C. Coenen, M. Jorgensen, D. M. Tanenbaum, F. C. Krebs, H. Gorter, S. Sabik, L. H. Slooff, S. C. Veenstra, J. M. Kroon, R. Andriessen, *Adv. Energy Mater.* **2012**, *2*, 103.
[7] Y. Guillou, A-M. Dutron, *Proc. IEEE Europ. Microelectron. Packag. Conf.* **2009**, 1.

© 2014 WILEY-VCH Verlag GmbH & Co. KGaA, Weinheim

[8] D. Huang, F. Liao, S. Molesa, D. Redinger, V. Subramanian, *J. Electrochem. Soc.* **2003**, *150*, G412.
[9] C. F. Luk, Y. Chan, K. Hung, *Microelectron. Reliab.* **2002**, *42*, 381.
[10] J. Jordan, *Proc. IEEE/CPMT/SEMI Int. Electron. Manuf. Technol. Symp., 27th* **2002**, 110.
[11] A. Yeoh, M. Chang, C. Pelto, T-L. Huang, S. Balakrishnan, G. Leatherman, *Proc. Electron. Compon. Technol. Conf.* **2006**, 1611.
[12] M. Huang, O. G. Yeow, C. Y. Poo, T. Jiang, *IEEE Trans. Comp., Packag. Technol.* **2008**, *31*, 767.
[13] S. Joblot, P. Bar, H. Sibuet, B. Reig, S. Jan, C. Arnaud, Y. Lamy, P. Coudrain, R. Coffy, O. Boillon, J. F. Carpenter, *Microelectron. Eng.* **2013**, *107*, 72.
[14] F. Wang, L. Han, *IEEE Tran. Compon., Packag., Manuf. Technol.* **2013**, *3*, 930.
[15] Y. Li, Y. Wu, B. Ong, *J. Am. Chem. Soc.* **2005**, *127*, 3266.
[16] A. Kamyshny, J. Steinke, S. Magdassi, *Open Appl. Phys. J.* **2011**, *4*, 19.
[17] S. K. Volkman, S. Yin, T. Bakhishev, K. Puntambekar, V. Subramanian, M. F. Toney, *Chem. Mater.* **2011**, *23*, 4634.
[18] P. Buffat, J-P. Borel, *Phys. Rev. A.* **1976**, *13*, 2287.
[19] J. S. Kang, J. Ryu, H. S. Kim, H. T. Hahn, *J. Electron. Mater.* **2011**, *40*, 2268.
[20] J. Perelaer, B-J. de Gans, U. S. Schubert, *Adv. Mater.* **2006**, *18*, 2101.
[21] M. Hummelgard, R. Zhang, H.-E. Nilsson, H. Olin, *PLoS One* **2011**, *6*, e17209.
[22] T. Bakhishev, V. Subramanian, *J. Electron. Mater.* **2009**, *38*, 2720.
[23] ITRS, *International Technology Roadmap for Semiconductors – Assembly and Packaging*, http://itrs.net/ (accessed: February, 2014).
[24] J. Sadie, S. K. Volkman, V. Subramanian, *Proc. Int. Symp. Microelectron., 46th* **2012**, 419.
[25] K. Murata, *IEEE. Int. Conf. Poly. Adhes. Microelectron. Photonics, 6th* **2007**, 293.
[26] J. A. Lewis, *Adv. Func. Mater.* **2006**, *16*, 2193.
[27] D. B. Wallace, D. J. Hayes, *Int. J. Microcircuits Electro. Packag.* **1998**, *21*.
[28] J. R. Greer, R. A. Street, *Acta Mater.* **2007**, *55*, 6345.
[29] National Institute of Standards and Technology, Database for Solder Properties with Emphasis on New Lead-Free Solders, http://www.msed.nist.gov/solder/ (accessed: June, 2014).
[30] JEDEC, JESD22-B117A Solder Ball Shear, http://www.jedec.org/ (accessed: February, 2014).
[31] AdvanPack Solutions Pte. Ltd., Products and Services, http://www.advanpack.com/ (accessed: February, 2014).
[32] R. Anderson, S. J. Klepeis, in *Introduction to Focused Ion Beams* (Eds: L. A. Giannuzzi, F. A. Stevie), Springer, Boston, MA, USA **2005**, Ch. 9.

© 2014 WILEY-VCH Verlag GmbH & Co. KGaA, Weinheim